Available online at www.sciencedirect.com
ScienceDirect
Comput. Methods Appl. Mech. Engrg. 362 (2020) 112873
Computer methods in applied mechanics and engineering
www.elsevier.com/locate/cma

Fourier series-based discrete element method for computational mechanics of irregular-shaped particles

Zhengshou Lai[a], Qiushi Chen[b,*], Linchong Huang[c]

[a] School of Intelligent Systems Engineering, Sun Yat-sen University, Guangzhou, 510275, China
[b] Glenn Department of Civil Engineering, Clemson University, Clemson, SC, 29634, USA
[c] School of Aeronautics and Astronautics Engineering, Sun Yat-sen University, Guangzhou, 510275, China

Received 19 February 2019; received in revised form 21 August 2019; accepted 20 January 2020
Available online xxxx

Abstract

Many natural and engineered granular materials consist mainly of irregular-shaped non-spherical particles. In this work, a novel Fourier series-based Discrete Element Method (FS-DEM) is developed for the computational mechanics of irregular-shaped particles. In FS-DEM, Fourier series-based particle geometric description and coordinate representation are introduced, where particle shapes are implicitly determined by FS coefficients, which remain constant and are independent of particle positions or kinematics. Using the FS-based particle representation, contact detection and resolution algorithms are then developed to identify contacts and resolve contact geometric features. The FS-DEM method is completed with recourse to conventional contact behavior, laws of motion, and movement integration. The accuracy and computational efficiency of the FS-DEM framework are evaluated via three numerical examples and compared with the Overlapping Discrete Element Cluster-based DEM method. Results demonstrate the robust and superior performance of the FS-DEM method and its potential for efficient computational modeling of irregular-shaped particle systems.

Keywords: Discrete element method; Irregular shapes; Fourier series; Contact detection and resolution; Granular materials

1. Introduction

Constituent particles of many natural and engineered granular materials, such as sands, biomass particles, and pharmaceutical pills, are non-spherical in general. Particle shapes are known to significantly impact the mechanical behavior of the bulk granular materials [1–4]. In conventional discrete element method (DEM) [5], idealized shapes (discs in two dimensions and spheres in three dimensions) have been adopted to model individual particles as it is simple and computationally efficient to detect contact points and resolve contact features (i.e., contact normal and tangential directions, contact branch vector, and contact overlapping length). Such simplification, however, ignores the effect of particle shapes and can significantly underestimate the strength of the bulk granular material. For example, it is shown in a recent study by Lai and Chen [6] that the particle shape effects accounted for approximately 40% of the shear resistance of a granular geomaterial. Peña et al. [2] studied the influence of particle shape on

* Corresponding author.
E-mail address: qiushi@clemson.edu (Q. Chen).

https://doi.org/10.1016/j.cma.2020.112873

the global mechanical behavior of dense granular media and discovered that the shear band width depends on the particle shape due to the tendency of elongated particles to develop preferential orientations and exhibit less rotation. A DEM model capable of accounting for realistic particle shapes is desired to realistically simulate and predict the behavior of granular materials.

Depending on how an irregular shape is represented, the DEM method for irregular-shaped particles can be classified into two groups, i.e., the single-particle method and the composite-particle method [7]. The single-particle method models individual irregular-shaped particle using closed geometries. Many single-particle-based DEM models have been proposed, and various closed geometries are adopted, including cylinder [8], polyhedron (or polygon in 2D) [9,10], ellipsoid (or ellipse in 2D) [11,12], oval (in 2D) [13], Non-Uniform Rational Basis Spline (NURBS) [14], and combinations of several closed geometries [15,16]. The application of the cylinder-based or ellipsoid-based DEM models is limited due to the particular particle shapes they can represent. The polyhedron-based DEM model is able to replicate arbitrary particle shapes. The accuracy of the shape represented by polyhedra improves with the number of faces in a polyhedron, but a large number of faces would lead to a higher computational cost. Moreover, polyhedron can rarely replicate a smooth particle shape. The NURBS-based granular element method (GEM) by Andrade et al. [14] could replicate general and smooth particle shapes but is computationally expensive. Another type of single-particle-based DEM is the LS-DEM recently proposed by Kawamoto et al. [17]. The LS-DEM seamlessly utilizes the level set data of realistic particle shapes characterized by X-ray computed tomography and is computationally efficient. One main limitation with LS-DEM is its high memory demand due to the need to store values of the level set function at every grid point, as noted in the original LS-DEM paper by [17], which could affect its application to large granular material systems.

For the composite-particle method, an irregular-shaped particle is represented by compositions of basic shapes, e.g., discs in 2D and spheres in 3D [18,19]. The composite-particle method is advantageous for implementation as the contact detection and resolution algorithms of the constituent basic shapes can be easily exploited. It is a prevalent method to model irregular particles in DEM [6,19–22] and is supported by commercial and open-source DEM packages such as PFC [23] and LIGGGHTS [24]. The accuracy of the composite-particle method is affected by the number of simple geometries used to represent an irregular particle, where a larger number of simple geometries is more accurate but would lead to greater computational expenses. Moreover, the composite-particle-based DEM model cannot reproduce smooth particle shapes.

The Fourier series (FS) method for particle shape representation has been a research topic in geomechanics for decades [25–29]. It has been shown to be an accurate and robust technique for describing and characterizing particle shapes. With advances in computed tomography and image analysis technologies, there has been increasing research interests in FS-based particle shape representation [30–35]. In the FS method, particle shape is simply determined by constant FS coefficients and no vertex or control points are required as in the polyhedron or NURBS methods. FS can successfully reproduce precise particle micromorphology in terms of shape irregularity and surface texture. Moreover, the shape represented using the FS method is smooth, continuous, and differentiable. Thus, its mass and moment of inertia can be easily derived as closed-form expressions, a convenient feature for evaluating particle motions. The FS-based method has also been used to track particles in a realistic experiment with the aid of X-ray imaging technique [36]. Although the FS method shows great advantages and potentials in representing realistic irregular-shaped granular particles, its application in DEM is an opportunity yet to be explored. This work, therefore, aims to develop a novel Fourier series-based Discrete Element Method (FS-DEM) for computational mechanics of irregular-shaped particles.

In a typical DEM calculation cycle, four key steps are generally involved: (1) resolving contact features, (2) evaluating contact behavior, (3) calculating particle motion, and (4) updating particle geometric description. This paper is devoted to presenting the methodology and algorithm details in each step of the proposed FS-DEM method. First, the FS-based method for the shape description and coordinate representation of particles is introduced. The separation of shape and coordinate descriptors is advantageous to algorithmic implementation and computational efficiency (e.g., in updating the particle geometric description). Algorithms for detecting contacts and resolving the contact geometric features are then developed. The contact geometric features include contact normal and tangential direction, contact branch vector and contact overlapping length, which are the bases to evaluate the contact behavior (i.e., contact forces and moments) in a DEM simulation. For the calculation of contact behavior and particle motion, the current FS-DEM framework exploits corresponding algorithms in existing DEM models with minor modifications. The utilization of existing algorithms facilitates the development and implementation

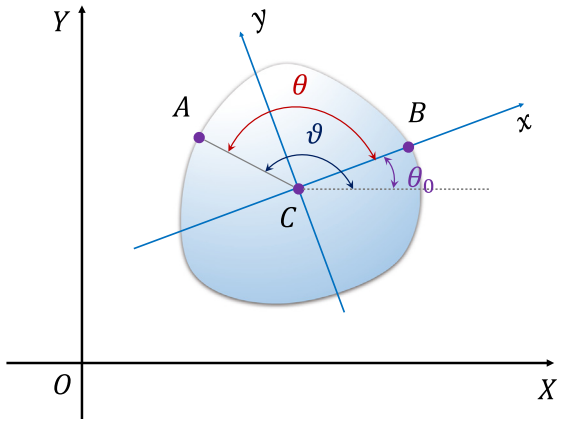

Fig. 1. Illustration of the local and global coordinate systems for an irregular particle.

of FS-DEM. Lastly, the relation between the position descriptors and the particle kinematics is presented, for the calculation of particle geometric position in the last step. It should be pointed out that this work has focused its discussion on 2D models, and the extension of the current FS-DEM framework to 3D models will be explored in future work.

2. FS-based particle description

The first key component of the proposed FS-DEM method is the particle shape representation. In this section, we present the FS-based particle geometric description and coordinate representation, followed by closed-form expressions for calculating particle mass and moment of inertia in FS-DEM.

2.1. Particle geometric description and coordinate representation

In the FS method, a particle is fully described by its two sets of geometric descriptors: shape descriptors and position descriptors. As shown in Fig. 1, there are two coordinate systems involved in describing particle geometry, a global coordinate system denoted by X-Y, and a local coordinate system, denoted by x-y. Given an irregular-shaped particle, the local x-y coordinate system is established with its origin C at the particle centroid and the x-axis pointing to a fixed but otherwise arbitrary point B on the particle surface. This local coordinate system moves with the particle as the particle is translated or rotated. In the local coordinate system, any point on the particle surface can be determined by its radial distance r with respect to the origin and its polar angle θ with respect to the x-axis, as illustrated in Fig. 1. Thus, the local coordinates (x_A, y_A) of any point A on the particle surface can be expressed as

$$x_A = r\cos\theta \tag{1}$$

$$y_A = r\sin\theta \tag{2}$$

The radial distance r can be approximated by a Fourier series expansion, given by

$$r(\theta) = \frac{1}{2}a_0 + \sum_{n=1}^{N}\left[a_n\cos(n\theta) + b_n\sin(n\theta)\right] \tag{3}$$

where a_0, a_n and b_n are the Fourier coefficients; $N \geq 1$ is the order of the Fourier series expansion. Using a more compacted vector form, Eq. (3) can be written as

$$r(\theta) = \mathcal{T}_{FS}(\theta)\cdot\mathcal{C}_{FS} \tag{4}$$

where $\mathcal{T}_{FS}(\theta) = [\frac{1}{2}, \cos(\theta), \sin(\theta), \ldots, \cos(N\theta), \sin(N\theta)]$ denotes the Fourier basis functions and $\mathcal{C}_{FS} = [a_0, a_1, b_1, \ldots, a_N, b_N]$ denotes the Fourier coefficients. The above r-θ approach has the issue of re-entrant angles,

i.e., it is possible to have multiple values of r for a given θ. There are other FS-based approaches that can mitigate this issue, e.g., the Fourier descriptor analysis approach [29], and the circle-mapping approach [35]. However, the r-θ approach is adopted due to two key advantages: (1) the polar angle can be directly related to the particle rotation without any further transformation, and (2) the contact detection and evaluation problem can be converted to an equivalent root-solving problem with only one variable θ

For particles represented using the FS method, closed-form expressions for mass and moment of inertia can be easily derived and will be shown in the next section.

The global coordinates (X_A, Y_A) of point A can be calculated via the following coordinate transformation

$$X_A = X_C + r(\theta)\cos\vartheta \tag{5}$$

$$Y_A = Y_C + r(\theta)\sin\vartheta \tag{6}$$

where X_C and Y_C are the global coordinates of point C (see Fig. 1); θ is the angle from the positive x-axis to $\overrightarrow{CA}$ (counterclockwise as positive); $\vartheta = \theta + \theta_0$ is the angle from the positive X-axis to $\overrightarrow{CA}$ with θ_0 denoting the angle from the positive X-axis to the positive x-axis.

The above expression of Eqs. (5) and (6) shows that any point A on the particle surface can be determined by a set of parameters $\{\mathcal{C}_{FS}, X_C, Y_C, \theta_0\}$. Among them, the Fourier coefficients $\mathcal{C}_{FS}$, termed shape descriptors hereafter, remain constants and are independent of the particle position and particle motion or kinematics. The other three parameters X_C, Y_C, and θ_0, termed position descriptors hereafter, are directly related to the particle motion, i.e., X_C and Y_C characterize the particle translation, and θ_0 characterizes the particle rotation. It should be noted that the presented FS method is only applicable to convex particles and the discussion hereafter is therefore limited to convex particles. Also, no particle breakage is considered in this work.

2.2. Particle mass and moment of inertia calculations

Using the radial distance r and polar angle θ, the mass m and the moment of inertia I_m of a particle can be expressed as

$$m = \rho \int_0^{2\pi} \int_0^{r(\theta)} r dr d\theta \tag{7}$$

$$I_m = \rho \int_0^{2\pi} \int_0^{r(\theta)} r^2 \cdot r dr d\theta \tag{8}$$

where ρ is particle density. In the FS method, the radial distance $r(\theta)$ can be approximated by a Fourier series expansion, as given in Eq. (3). Substituting Eq. (3) into Eq. (7) yields the following closed-form expressions for calculating the mass and moment of inertia of a particle in FS-DEM

$$m = \rho\pi\,(c_1/4 + c_2/2) \tag{9}$$

$$I_m = \rho\pi\left(c_3/32 - 9c_4/16 + 3c_1c_2/8 + 3c_2^2/4\right) \tag{10}$$

where $c_1 = a_0^2$, $c_2 = \sum_{k=1}^{N}(a_k^2 + b_k^2)$, $c_3 = a_0^4$, $c_4 = \sum_{k=1}^{N}(a_k^4 + b_k^4)$, $a_0, \ldots, a_k$ are the Fourier coefficients, and N is the order of the Fourier series expansion.

3. Contact detection and resolution

At the core of a DEM model are the contact detection and contact resolution algorithms. Contact detection refers to identifying whether or not two particles (or a particle and a boundary) are in contact. Contact resolution refers to resolving contact geometric features that are used in evaluating contact forces. In this section, we present the contact detection and resolution algorithms for the particle–particle case and the particle–boundary case.

3.1. Particle–particle contact

3.1.1. Contact detection

Fig. 2 illustrates the possible scenarios in the contact detection of two particles p and q, the centroids of which are located at points C_p and C_q. Point A_p is an arbitrary point on the surface of particle p. The angle from the

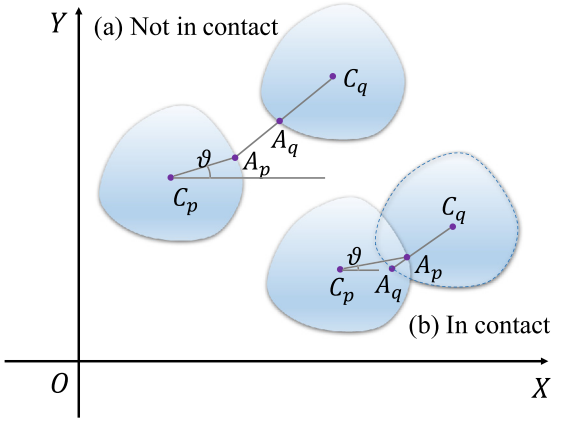

Fig. 2. Illustration of particle–particle contact scenarios and key geometric parameters.

positive X-axis to $\overrightarrow{C_pA_p}$ is denoted as ϑ. Line C_qA_p intersects the surface of particle q at point A_q. The signed distance between points A_p and A_q is defined as

$$\mathcal{D} = \mathcal{L}_{C_qA_p} - \mathcal{L}_{C_qA_q} \tag{11}$$

where $\mathcal{L}_{[\cdot]}$ denotes the length of line segment $[\cdot]$.

With the definition in (11), the minimum value of $\mathcal{D}$ is an indicator of whether or not the two particles are in contact, i.e., $\mathcal{D}_{\min} \leq 0$ indicates particles are in contact and $\mathcal{D}_{\min} > 0$ indicates particles are not in contact. Therefore, the contact detection problem can be equivalently approached by solving a constrained minimization problem

$$\min_{\vartheta} \mathcal{D}(\vartheta) \leq 0, \quad \vartheta \in [0, 2\pi] \tag{12}$$

Problem (12) can be solved via various algorithms, such as the gradient-based Newton's method, the stochastic searching-based Particle Swarm Optimization (PSO) method [37,38], and the Nelder–Mead simplex algorithm [39,40]. The gradient-based Newton's method is the most commonly used and will be adopted in this work. Details of the algorithm are included in Appendix A.1.

3.1.2. Contact resolution

Once two particles are detected to be in contact by Eq. (12), the contact geometric features will need to be resolved. Currently, there lacks a general contact theory for irregular-shaped particles in DEM [8], and therefore, the contact geometric features need to be defined first for FS-based particle representation. The contact model adopted in this work is the widely used spring-based contact model [5], in which the following contact geometric features are involved: the contact normal direction $\boldsymbol{n}$ and the tangential direction $\boldsymbol{t}$; the branch vector $\boldsymbol{b}$ that goes from the particle centroid to the contact point; the normal overlapping length δ_n and the tangential overlapping length increment $\Delta\delta_t$.

The starting point of contact resolution is to determine the intersections of the two particles in contact. As illustrated in Fig. 3, the intersections of two contacting particles, p and q, are denoted as I_1 and I_2. The coordinates of the first intersection I_1 can be obtained by solving the following problem

$$\mathcal{D}(\vartheta_{I_1}) = 0, \quad \vartheta \in [\vartheta_l, \vartheta_u] \tag{13}$$

where $\mathcal{D}$ is the signed distance function defined in Eq. (11); ϑ_{I_1} is the variable that determines the coordinates of point I_1; ϑ_l and ϑ_u are the lower and upper bounds of variable ϑ_{I_1}, respectively. A simple choice for the lower and upper bounds is to set ϑ_l to the solution of problem (12) and set $\vartheta_u = \vartheta_l + \pi$. Alternatively, a narrower range for the lower and upper bounds can be obtained based on the sampling grid used when solving Eq. (12) by Newton's method.

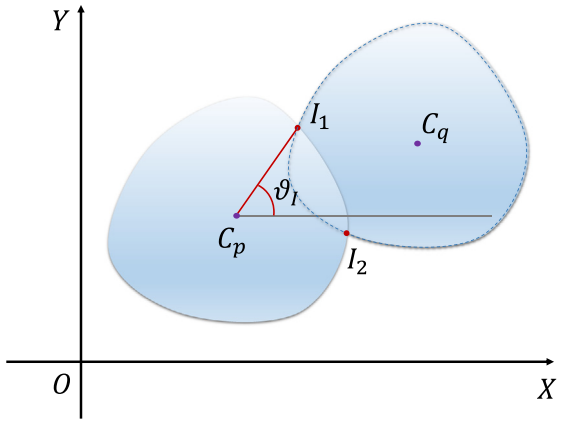

Fig. 3. Illustration of two particles in contact: centroids of the two particles are denoted as C_p and C_q; I_1 and I_2 are two contacting points; ϑ_I is the angle of contact points with respect to the horizontal direction.

To solve problem (13), a combined bisection and Newton's method is implemented in this work, which leverages the guaranteed convergence of the bisection method and the quadratic convergence rate of Newton's method. The detailed algorithm of the combined bisection and Newton's method is presented in Algorithm 1. Problem (13) is repeated to determine the other intersection I_2.

Algorithm 1: The combined bisection and Newton's method for determining intersections of two particles in contact

Input : Particle shape and position descriptors: $\{\mathcal{C}_{FS}^p, X_C^p, Y_C^p, \theta_0^p\}$, $\{\mathcal{C}_{FS}^q, X_C^q, Y_C^q, \theta_0^q\}$;
Initial guess of the lower bound and upper bound: ϑ_l and ϑ_u;
Maximum iterations in Newton's method $k_{\max}$ and tolerance ϵ.
Output: The root of problem (13): ϑ_I

Initialize $\vartheta^0 = (\vartheta_l + \vartheta_u)/2$, $\Delta\vartheta = 0$
for $k \leftarrow 1$ **to** $k_{\max}$ **do**
  $\vartheta^k = \vartheta^{k-1} + \Delta\vartheta$
  if $\vartheta^k \notin [\vartheta_l, \vartheta_u]$ **then**
    $\vartheta^k = (\vartheta_l + \vartheta_u)/2$
  end
  if $\mathcal{D}(\vartheta^k) < -\epsilon$ **then**
    $\vartheta_l = \vartheta^k$
  else if $\mathcal{D}(\vartheta^k) > \epsilon$ **then**
    $\vartheta_u = \vartheta^k$
  else
    $\vartheta_I = \vartheta^k$ **break**
  end
  $\Delta\vartheta = -\{\frac{\partial\mathcal{D}}{\partial\vartheta}|_{\vartheta^k}\}\backslash\{\mathcal{D}(\vartheta^k)\}$
end
if $k == k_{\max}$ **then**
  display the non-convergence warning
end

Once the two contact intersections I_1 and I_2 are determined, an effective contact point can be obtained. The effective contact point will be used to calculate the contact normal and tangential directions, the contact branch vectors, and the contact normal overlapping length. As shown in Fig. 4, in this work, the effective contact point M is defined as the midpoint of the two intersections I_1 and I_2. Then, the contact tangential direction $\boldsymbol{t}$ is defined as the direction of $\overrightarrow{I_1 I_2}$ and the contact normal direction $\boldsymbol{n}$ is the contact tangential direction rotated clockwise by 90°.

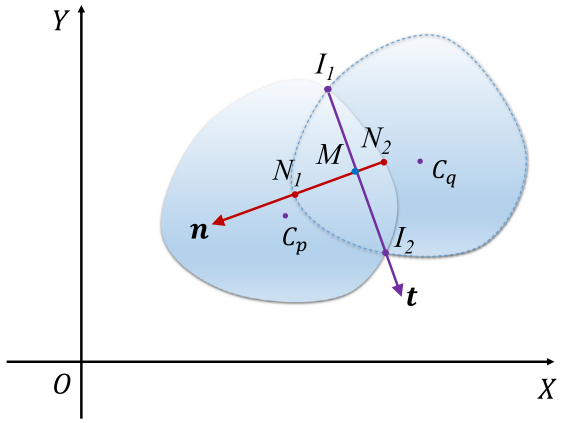

Fig. 4. Contact geometric features for the case of particle–particle contact.

The contact branch vector $\boldsymbol{b}$, by definition, is $\overrightarrow{MC}_p$ or $\overrightarrow{MC}_q$, accordingly. It is worth mentioning that a similar set of definitions for these contact geometric features were adopted by Andrade et al. [14] for their proposed granular element method.

To evaluate the contact overlapping lengths, a line passing the effective contact point M and parallel to the contact normal direction $\boldsymbol{n}$ is defined. This line intersects with each particle surface at points N_1 and N_2. The algorithm for determining the coordinates of points N_1 and N_2 is detailed in Appendix B. The normal overlapping length δ_n is then defined as the length of line segment $\overrightarrow{N_1N_2}$

$$\delta_n = \mathcal{L}_{N_1N_2} \tag{14}$$

where $\mathcal{L}_{[\cdot]}$ denotes the length of line segment $[\cdot]$. The tangential overlapping length increment $\Delta\delta_t$ is calculated as

$$\Delta\delta_t = v_t \Delta t \tag{15}$$

where v_t is the relative tangential velocity of one particle with respect to the other particle; Δt is the current time increment. The relative tangential velocity v_t is calculated as

$$v_t = (\boldsymbol{v}^p - \boldsymbol{v}^q) \cdot \boldsymbol{t} - (\omega^p l_n^p + \omega^q l_n^q) \tag{16}$$

where $\boldsymbol{v}$ and ω are the translational velocity and rotational velocity of particles, respectively; $l_n = |\boldsymbol{b} \cdot \boldsymbol{n}|$ is the length of the branch vector projected to the contact normal direction; $\boldsymbol{t}$ is the contact tangential direction. The superscripts $[\cdot]^p$ and $[\cdot]^q$ in the equation indicate the variables belonging to particle p or q, respectively. The subscripts $[\cdot]_n$ and $[\cdot]_t$ indicate the normal and tangential components of the variable, respectively.

3.2. Particle–boundary case

3.2.1. Contact detection

As in most conventional DEM models, boundaries can be represented by lines (or approximated by a series of line segments), expressed as

$$X \sin\alpha - Y \cos\alpha + c = 0 \tag{17}$$

where $\alpha \in [0, \pi)$ is the angle of the boundary line; c is a parameter indicating the signed distance from the origin to the boundary.

Fig. 5 illustrates the two scenarios of particle–boundary contact. Point A is an arbitrary point on the surface of the particle and the signed distance $\mathcal{L}_A$ from point A to the boundary can be defined as

$$\mathcal{L}_A = X_A \sin\alpha - Y_A \cos\alpha + c \tag{18}$$

where X_A and Y_A are the global coordinates of point A and can be further expressed as functions of ϑ_A via Eqs. (5) and (6). Thus, $\mathcal{L}_A$ is eventually a function of ϑ_A.

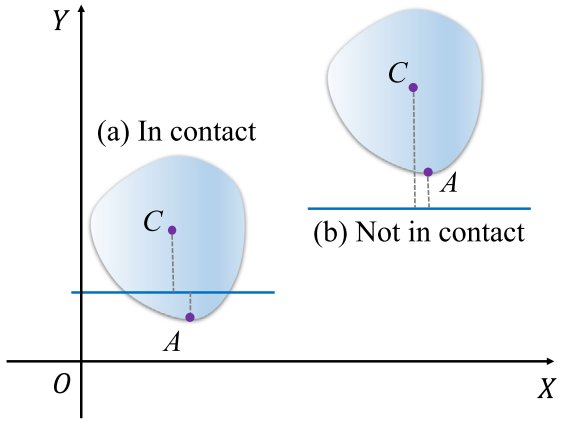

Fig. 5. Illustration of particle–boundary contact scenarios. C is the centroid and A is an arbitrary point on the particle surface.

As shown in Fig. 5, if the particle is in contact with the boundary, there should exist a point A on the surface of the particle such that point A and the particle centroid C are on the opposite sides of the boundary. Thus, the signed distances of point A and C to the boundary have different signs. Define the product of the signed distances $\mathcal{L}_A$ and $\mathcal{L}_C$ as

$$\mathcal{P} = \mathcal{L}_C \mathcal{L}_A \tag{19}$$

The minimum value of $\mathcal{P}$ is an indicator of the particle–boundary contact status. If $\mathcal{P}_{\min} \leq 0$, the particle and boundary are in contact. If $\mathcal{P}_{\min} > 0$, the particle and boundary are not in contact. Similar to the particle–particle contact case, contact detection can be approached by solving a constrained minimization problem

$$\min_{\vartheta_A} \mathcal{P} \leq 0, \quad \vartheta \in [0, 2\pi] \tag{20}$$

Again, Newton's method is adopted in this work to solve this minimization problem (20) and the algorithm is detailed in Appendix A.2.

3.2.2. Contact resolution

Fig. 6 shows the example in which a particle and a boundary are in contact. Assume point A is the point that corresponds to $\mathcal{P}_{\min}$. The line connecting point A and the particle centroid C intersects the boundary line at point N. The midpoint M of line segment AN is defined as the contact point for the case of particle–boundary contact. The contact normal direction is normal to the boundary and pointing to the particle centroid side. The contact tangential direction is the contact normal direction rotated by 90° counterclockwise. The contact branch vector $\boldsymbol{b}$, in this case, is $\overrightarrow{MC}$.

The normal overlapping length is defined as the magnitude of signed distance $\mathcal{L}_A$, i.e., the distance from point A to the boundary, written as

$$\delta_n = |\mathcal{L}_A| \tag{21}$$

The tangential overlapping length increment $\Delta\delta_t$ for the case of particle–boundary contact is also calculated using Eq. (15). However, the calculation of the relative tangential velocity v_t is slightly different as

$$v_t = (\boldsymbol{v}^p - \boldsymbol{v}^b) \cdot \boldsymbol{t} - (\omega^p l_n^p + \omega^b l_n^b) \tag{22}$$

where $\boldsymbol{v}$ and ω are the translational and rotational velocity, respectively; l_n^b is the distance from the contact point to the boundary rotational center projected to the contact normal direction; l_n^p is the length of the branch vector projected to the contact normal direction; $\boldsymbol{t}$ is the contact tangential direction. The superscripts $[\cdot]^p$ and $[\cdot]^b$ indicate the variable belonging to the particle and the boundary, respectively.

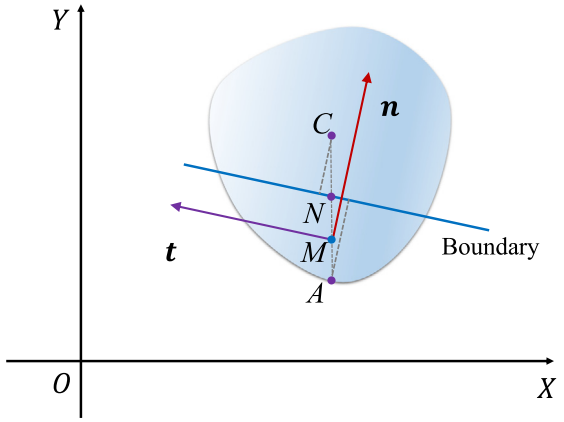

Fig. 6. Contact geometric features for the type of particle–boundary contact.

4. Framework of the FS-DEM

With the key components described in the previous two sections, we complete the proposed FS-DEM framework in this section.

4.1. Workflow and key steps

Fig. 7 shows the workflow and calculations that are involved in one typical calculation cycle of the FS-DEM framework. The calculations in each cycle can be grouped into four steps:

Contact features The FS-DEM differs from the existing DEM in the step of resolving contact features, where the FS-based method for particle geometric description and coordinate representation is adopted. The algorithms for resolving contact features have been addressed in Section 3.

Contact behavior For evaluating contact behavior (i.e., the contact forces and moments), most of the existing contact models, e.g., the linear contact model [5], the Hertz contact model [41,42], and the rolling resistance contact model [43], can be directly exploited by the FS-DEM framework.

Particle motion This step involves calculating particle motions (i.e., acceleration and velocity) based on the forces and moments acting on the particle. The FS-DEM can also adopt the same law of motion in existing DEM for this step.

Particle geometric description In this step, the FS-DEM framework exhibits great efficiency by only requiring updating a few variables (i.e., the position descriptors X_C, Y_C and θ_0 in Eqs. (5) and (6)). The particle shape descriptors (i.e., the FS coefficients in Eq. (4)) remain constant and are independent of the particle motion and kinematics. As a comparison, other DEM models such as the Polygon-based [10] and the ODEC-based [18] models require updating of polygon vertices and the centroid of particles in a clump at each cycle, leading to greater computational cost.

In the current FS-DEM framework, the linear contact model [5] for contact behavior and the second-order Velocity Verlet algorithm [44] for solving particle motion are adopted. For completeness, the linear contact model and the Velocity Verlet algorithm are briefly presented in the following sections.

4.2. Contact behavior

The spring-based contact theory is adopted in this work. The action of one particle (or boundary) on another at the contacts is generalized into the contact force and contact moment. The contact force $\boldsymbol{F}_c$ consists of two parts: the normal force $\boldsymbol{F}_n$ and the tangential force $\boldsymbol{F}_t$

$$\boldsymbol{F}_c = \boldsymbol{F}_n + \boldsymbol{F}_t = F_n\boldsymbol{n} + F_t\boldsymbol{t} \tag{23}$$

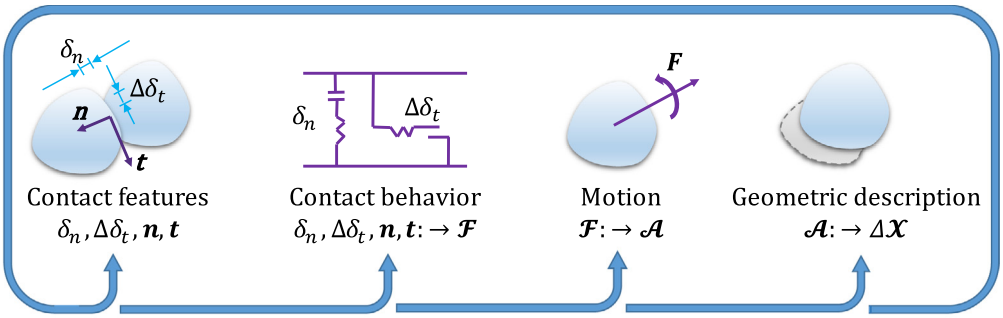

Fig. 7. The workflow and calculations that are involved in one typical cycle of the FS-DEM framework.

where $\boldsymbol{n}$ and $\boldsymbol{t}$ are the normal vectors indicating the contact normal and tangential direction, respectively; F_n and F_t are the magnitudes of contact normal and tangential forces, respectively.

The contact normal force is evaluated based on the normal overlapping length and the tangential force is evaluated based on the tangential overlapping length increment. The contact law for a simple linear model updates the contact forces and contact moment through [5]

$$F_n = k_n \delta_n \tag{24a}$$

$$F_t = \min(F_t^0 + k_t \Delta\delta_t, \mu_c F_n) \tag{24b}$$

$$M_c = 0 \tag{24c}$$

where k_n and k_t are the contact normal and tangential stiffness, respectively; μ_c is the contact friction coefficient; F_t^0 is the tangential force at the beginning of the current cycle; M_c is the contact moment. The contact moment is ignored here assuming non-rolling resistance in this simple linear contact model. It is worth noting that though the moment due to inter-particle rolling is not considered, there will be rolling moments that resulted from contact forces. As the particles are irregular, the contact forces may not pass the particle centroids and result in rolling moments with respect to the centroid. F_n, F_t and M_c are then converted to the force and moment F_X, F_Y and M in the global coordinate system.

4.3. Particle motion

For simplicity, a general variable $\mathcal{X}$ is defined to denote the particle translation and rotation such that $\mathcal{X} = \{X_C, Y_C; \theta_0\}$; and $\mathcal{V}$ is defined to denote the particle translational and rotational velocity such that $\mathcal{V} = \{v_{X_C}, v_{Y_C}; \omega_{\theta_0}\}$. The particle motion is governed by

$$\mathcal{M}\mathcal{A} + \mathcal{F}_d = \mathcal{F} \tag{25}$$

where $\mathcal{M} = \{m, m; I_m\}$ denotes the general mass, in which m represents the particle mass and I_m represents the particle moment of inertia; $\mathcal{A} = \{\dot{v}_{X_C}, \dot{v}_{Y_C}; \dot{\omega}_{\theta_0}\}$ denotes the general acceleration, in which the dot symbol indicates time derivative; $\mathcal{F} = \{F_X, F_Y; M\}$ denotes the general force, respectively; $\mathcal{F}_d$ is the local damping force. The local damping is introduced to facilitate the energy dissipation, expressed as

$$\mathcal{F}_d = \beta \mathcal{F} \text{sign}(\mathcal{V}) \tag{26}$$

Thus, the general form of acceleration can be expressed as

$$\mathcal{A} = \frac{(1 - \beta \text{sign}(\mathcal{V}))\mathcal{F}}{\mathcal{M}} \tag{27}$$

where β is the local damping coefficient. The sign function is defined as

$$\text{sign}(x) := \begin{cases} -1 & \text{if } x < 0 \\ 0 & \text{if } x = 0 \\ 1 & \text{if } x > 0 \end{cases} \tag{28}$$

4.4. Time integration and critical timestep

In the proposed FS-DEM framework, only the position descriptors of a particle need to be updated. The second order Velocity Verlet algorithm [44] is adopted in this work to update the particle position. Suppose that the current calculation cycle is at time t. The velocities at time t and $t + \Delta t/2$ are calculated as

$$\mathcal{V}^{t} = \mathcal{V}^{t-\Delta t/2} + \mathcal{A}^{t}\,\Delta t/2 \tag{29a}$$

$$\mathcal{V}^{t+\Delta t/2} = \mathcal{V}^{t-\Delta t/2} + \mathcal{A}^{t}\,\Delta t \tag{29b}$$

where Δt is the time increment at the current cycle; the superscripts $[\cdot]^{t-\Delta t/2}$, $[\cdot]^{t}$ and $[\cdot]^{t+\Delta t/2}$ denote the corresponding time. The position at time $t + \Delta t$ is updated as

$$\mathcal{X}^{t+\Delta t} = \mathcal{X}^{t} + \mathcal{V}^{t+\Delta t/2}\Delta t \tag{30}$$

The time integration based on the second-order Velocity Verlet algorithm is numerically stable only when the time increment being used is less than a threshold value, i.e., the critical timestep [45]. If a time increment greater than the critical timestep is used, particles may move too much in one increment, resulting in spuriously large overlaps and contact forces. A summary and assessment of different approaches to estimate the critical timestep for DEM simulations can be found in [45]. In [46], the criteria for quasi-static equilibrium DEM simulations and the selection of algorithmic parameters (i.e., critical timestep, damping coefficient, loading rate) were also discussed. In general, there are two categories of approaches to estimate the critical timestep: approaches based on the oscillation period of a single degree of freedom system (SDOF) [5,47], and the Rayleigh wave speed-based approaches [48,49].

For the SDOF-based approaches, Cundall and Strack [5] proposed the following expression to estimate the critical timestep Δt_{crit}

$$\Delta t_{\text{crit}} = \min\left(\sqrt{m/k^{\text{tran}}}, \sqrt{I_i/k_i^{\text{rot}}}\right) \tag{31}$$

where m is the mass of the particle; I_i is the moment of inertia of the particle; k^{tran} and k_i^{rot} represent the translational and rotational stiffness; the subscript i indicates the index of principal components.

For the Rayleigh wave speed-based approaches, Li et al. [49] proposed that

$$\Delta t_{\text{crit}} = \frac{\pi R\sqrt{\rho/G}}{0.1631\nu + 0.8766} \tag{32}$$

where R is the average particle radius; ρ is the particle density; G is the particle shear modulus; ν is the Poisson's ratio of the particle. The shear modulus and Poisson's ratio of particles can also be related to the particle normal and shear stiffness [46].

5. Numerical examples

In this section, three examples are presented to verify and to also demonstrate the performance of the FS-DEM framework. In the first example, the FS method is first applied to reproduce several irregular shapes. Then, the FS-based contact detection and resolution algorithms are applied to evaluate the contact between two irregular particles placed at random positions. To shed light on the accuracy and efficiency of the FS-DEM framework, the same tests using the Overlapping Discrete Element Cluster (ODEC) method [18] is also conducted as a comparison. The second example is a single-particle rockfall test, aiming to verify the accuracy of the FS-DEM framework. The results simulated in a commercial DEM code, PFC [23], are used as benchmarks. The effects of contact friction and contact damping are also investigated in these simulations. The last example is an oedometric compression test of multiple irregular particles, which aims to further demonstrate the capability and applicability of the FS-DEM framework.

5.1. Assessment of the computational performance

To evaluate its accuracy in particle shape description, the FS method is applied to represent a set of irregular shapes. As a comparison, the same test is conducted using the ODEC method. Fig. 8 displays the shape templates used in the following demonstrations. These shape templates are taken from a recent study [50], where particle

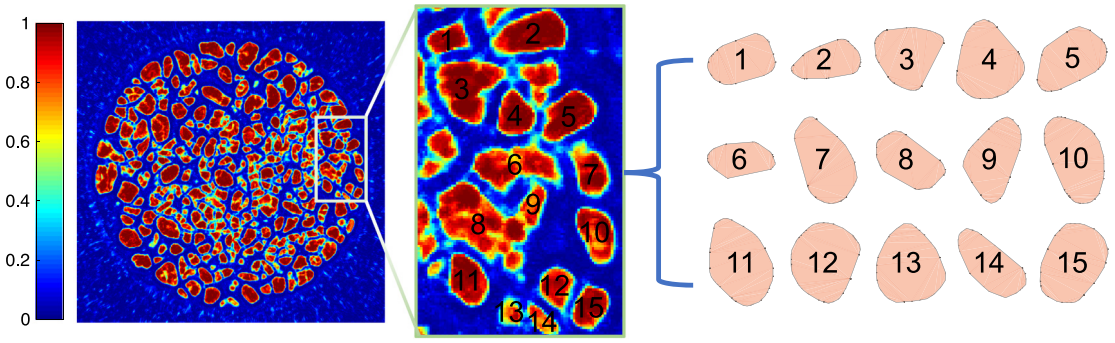

Fig. 8. The shape templates reconstructed from an X-ray CT image of Mojave Mars Simulant.

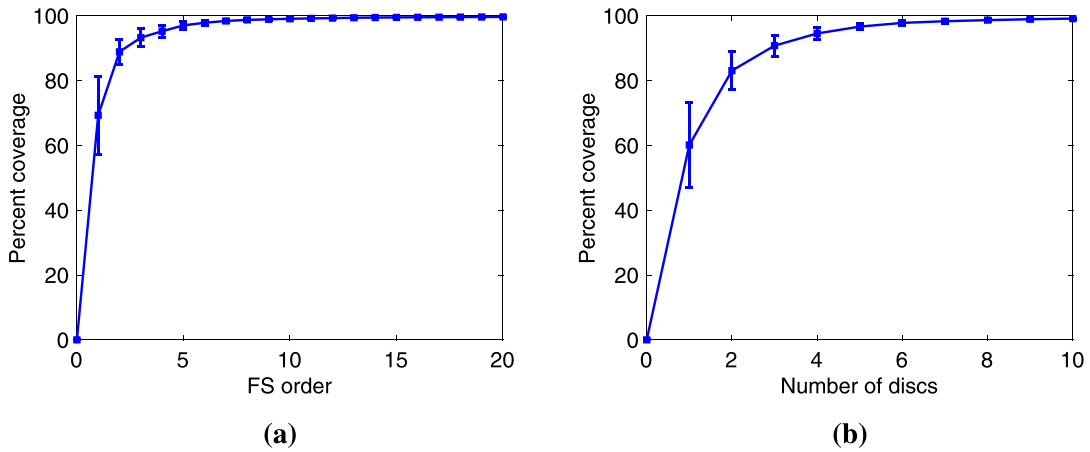

Fig. 9. The percent coverage as a function of (a) the FS order in the FS method, and (b) the number of discs in the ODEC method.

shapes are extracted and reconstructed from X-ray computed tomography (X-ray CT) images of Mojave Mars Simulant (MMS) using a novel machine learning-based framework. As this work focuses on convex particles, the original MMS shapes are made convex by extracting the convex hulls.

The percent coverage, defined as one minus the percent difference between the area of the reconstructed shape by the FS or ODEC method and the actual total area of the original shape, is introduced to quantify the accuracy of the FS or ODEC method in representing an irregular particle shape. Alternatively, the area ratio, which by definition is the percent ratio of the area of the cluster to the area of the original shape, can be used to quantify the accuracy, as has been adopted in the previous work of the ODEC method [18,51].

The results of the percent coverage for both methods are presented in Fig. 9. As the order of Fourier series expansion increases to 8, the FS method can achieve an averaged percent coverage of 98% or higher. For the ODEC method, approximately 6 or more discs are required to achieve the same percent coverage. Fig. 10 showcases the evolution of the covered area using FS and ODEC method.

Next, a simple test is performed to verify and demonstrate the performance of the FS-based contact detection and resolution algorithms developed in this work. The scenario of this test is shown in Fig. 11(a). In this test, one irregular-shaped particle (template 1 in Fig. 10) is fixed at the origin while a second irregular-shaped particle (template 4 in Fig. 10) is placed at a random position (i.e., random translational and rotational position) in a ring area bounded by two circles (shown as dashed line in Fig. 11(a)) with the center at the origin and a radius of 0.75 and 1.25, respectively. The irregular-shaped particles have an equivalent diameter of 1.0. Here, the equivalent diameter of a particle is defined as the diameter of a circular particle with the same area. Also, since no contact force will be calculated, no unit is used in this example. This scenario is expected to result in approximately 50% of contact cases if both particles are circles. The actual percentage of contact cases will deviate from 50% due

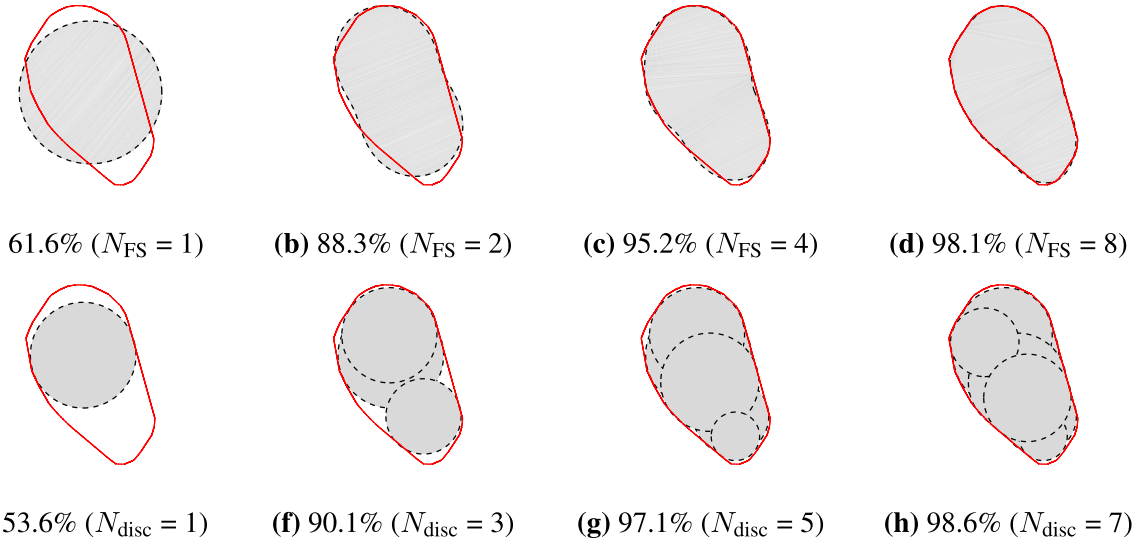

(a) 61.6% ($N_{\text{FS}} = 1$) **(b)** 88.3% ($N_{\text{FS}} = 2$) **(c)** 95.2% ($N_{\text{FS}} = 4$) **(d)** 98.1% ($N_{\text{FS}} = 8$)

(e) 53.6% ($N_{\text{disc}} = 1$) **(f)** 90.1% ($N_{\text{disc}} = 3$) **(g)** 97.1% ($N_{\text{disc}} = 5$) **(h)** 98.6% ($N_{\text{disc}} = 7$)

Fig. 10. The percent coverage evolution with increasing (a–d) Fourier series orders (N_{FS}), and (e–h) number of discs (N_{disc}). The solid red contour represents the reference shape and the dashed contours filled in gray represent the shape reproduced by the FS method or ODEC method.

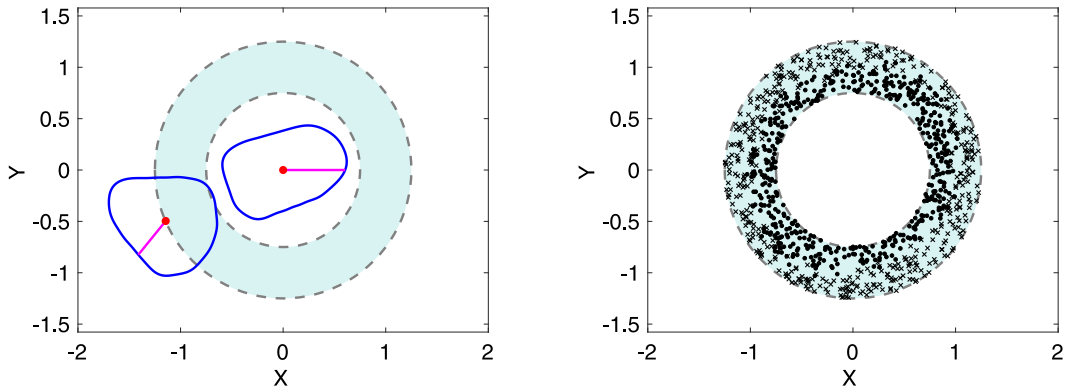

(a) **(b)**

Fig. 11. The contact evaluation scenario (a) one particle is fixed at the origin and a second particle is randomly placed in the shaded ring area (the red dot indicates the particle centroid and the pink line indicates the particle orientation); (b) results of contact detection for 10,000 random particle positions (solid dots indicate contact cases and crosses indicate non-contact cases).

to irregular particle shapes and the randomness of particle positions. The FS- and ODEC-based contact detection and resolution algorithms are applied to evaluate the contact between the two particles for 10,000 random particle positions.

The results of the 10,000 trials are summarized in Table 1. For both methods, the percentage of contact cases is about 50% (for all cases with 90% or more percent coverage) with reasonable deviations. Also, both methods yield similar *error* cases when the percent coverage is close. For example, for $N_{\text{FS}} = 5$ and $N_{\text{disc}} = 5$, the percent coverage is approximately 97.0%, which results in *error* cases of 1.89% and 1.77% for the FS and ODEC method, respectively. In terms of computational efficiency, the total run time for FS-based method increases approximately linearly with N_{FS}. The run time for the ODEC-based method, on the other hand, grows quadratically with the number of discs. When higher accuracy is required to describe particle shapes, the FS-based method exhibits superior computational performance compared to the ODEC-based method.

Table 1
Computational efficiency of contact detection by FS and ODEC methods.

Method	Percent coverage	Contact cases[a]	*Error* cases[a]	Run time (s)[b]
FS-based method				
FS order $N_{FS} = 5$	97.6%	53.8%	1.89%	4.8 (1.1 + 3.7)
FS order $N_{FS} = 10$	99.3%	53.9%	1.58%	5.5 (1.3 + 4.2)
FS order $N_{FS} = 15$	99.5%	53.8%	0.57%	6.1 (1.6 + 4.5)
ODEC-based method				
Disc number $N_{disc} = 1$	65.2%	20.0%	34.93%	1.0 (0.8 + 0.2)
Disc number $N_{disc} = 3$	92.9%	49.6%	5.52%	4.7 (2.3 + 2.4)
Disc number $N_{disc} = 5$	97.3%	53.4%	1.77%	11.2 (5.0 + 6.2)
Disc number $N_{disc} = 7$	98.9%	55.0%	2.42%	21.6 (8.7 + 11.9)

[a]Evaluated based on 10,000 trials.

[b]t_a ($t_b + t_c$), where t_a indicates the total time cost (for 10 000 trials), t_b indicates the time cost for all non-contact cases, and t_c indicates the time cost for all contact cases.

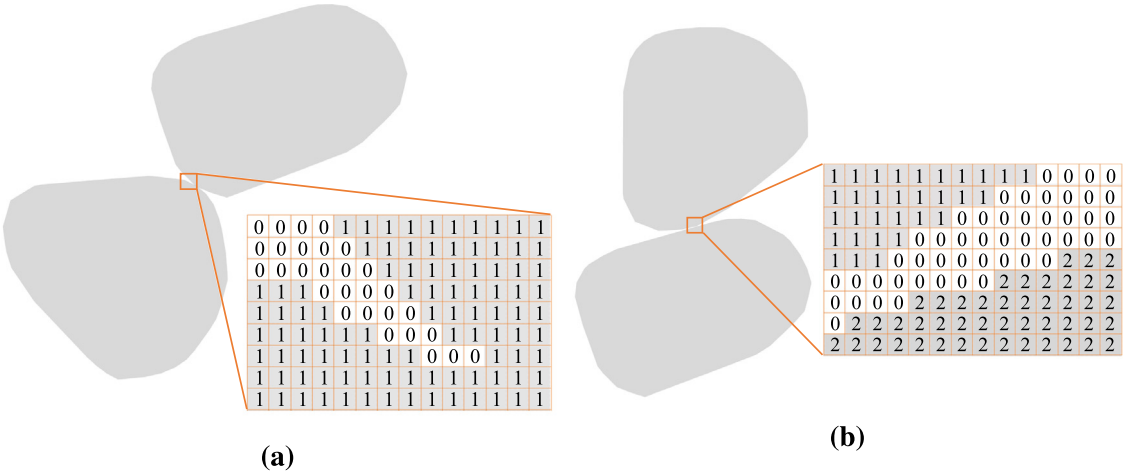

Fig. 12. Contact detection using image processing as a benchmark method: (a) contact case, and (b) non-contact case.

In Table 1, the error cases are obtained by comparing the contact result returned by the FS or ODEC method to the benchmark contact status. In this work, the benchmark contact status is obtained by an image analysis approach. In this approach, once two particles are generated and randomly placed, they are colored in grey and printed out as a binary image. The image is then imported and analyzed by an image labeling process in MATLAB. As illustrated in Fig. 12, if the image turns out to contain just one patch (i.e., the maximum label value is 1), the two particles are considered to be in contact (Fig. 12(a)). If the image turns out to contain two patches (i.e., the maximum label is 2), the two particles are considered to be not in contact (Fig. 12(b)). The pixels used in the binary image are set to be very small (a 1000 × 1000 grid is used per particle) to ensure that the contact status returned by the image analysis is sufficiently accurate and can be used as "true" contact status. If the contact status returned by the FS or ODEC method does not match the benchmark result, it is counted as an error case. It is worth noting that an error case does not mean the FS or ODEC method fails in detecting contacts correctly. The error cases are due to the accuracy of each method in describing the particle shapes. Also, it should be made clear that the image analysis approach is only used to provide benchmark contact status; it is not used by FS or ODEC for contact detection.

5.2. Single-particle rockfall simulations

In the second example, two sets of single-particle rockfall simulations are performed. The first set of simulations uses a disc-shaped particle so that the results of FS-DEM can be verified against the benchmark results simulated in PFC (using the ODEC method). The second set of simulations uses an irregular particle, based on which the

Table 2
Contact properties for single-particle rockfall simulations.

Case	Contact properties	
	Contact friction	Contact damping
I	0.0	0.0
II	0.2	0.0
III	0.2	0.2

particle shape effects on the rockfall process are demonstrated. In both cases, the particle is released above a slope and then allowed to fall down along the slope. During the falling, the particle successively collides with the slope.

5.2.1. Disc-shaped particle

For the first set of simulations, a disc-shaped particle with an equivalent diameter of 0.2 m is used. The density of the particle is 2700 kg/m^3. Both the contact normal and tangential stiffness k_n and k_s of the particle and slope are set to 8.5×10^7 N/m. Three cases with different contact friction and contact damping coefficients are considered as summarized in Table 2. The time-step size is fixed at 1×10^{-4} s.

The results simulated in PFC are used as benchmarks to verify the accuracy of the proposed FS-DEM method. It should be noted that, though the particle is simply a disc shape, the description of particle geometry, the detection of contact and the resolution algorithms in FS-DEM all differ from conventional DEM model implemented in PFC.

Figs. 13(a) and 13(b) display the particle trajectories simulated in FS-DEM and PFC (using the ODEC method) for case I, respectively. It is observed that the two methods give exactly the same results, i.e., the same particle trajectory and the same particle velocity. The energy evolution of the particle is shown in Fig. 13(c) (the energy results of PFC are not presented as they are identical to that of FS-DEM). As expected, the total energy of the particle remains the same during the simulation since there is no energy dissipation from contact friction or damping for case I. The sudden drops in the total energy happen when the particle collides the boundary and are caused by part of the energy being transferred to the elastic potential energy stored in the contact. Also, as there is no contact friction and the particle is ideally circular, the particle bears zero resultant rolling moment as expected, and therefore, the corresponding rotation energy remains zero throughout the simulation.

Particle trajectory and energy results for cases II and III are shown in Fig. 14. Again, results of FS-DEM and PFC (using the ODEC method) are in perfect agreement. It is observed that the particle trajectory and energy evolution are significantly affected by contact friction and damping. Due to the existence of contact friction, the particle is rotated as a result of the contact frictional force. In case II, the total energy drops at each collision and remains constant between collisions. In case III, the energy is dissipated not only via collisions but also via damping effects in every simulation cycle. Moreover, it is observed that the amount of energy dissipated by collisions in case III is larger than that in case II. Overall, it is observed that FS-DEM and PFC return identical results for the circular particle rockfall test regardless of what friction or damping coefficients are used. This is because for circular particles, both FS-DEM and PFC can represent the particle shape accurately. The contact features in FS-DEM and PFC are also calculated to be the same.

5.2.2. Irregular-shaped particle

In this section, an additional set of rock fall simulations is performed to evaluate the proposed FS-DEM method in modeling irregular-shaped particles. As a comparison, results by PFC (using the ODEC method) for irregular-shaped particles are also presented. The test setup is the same as the previous example. The irregular particle is created using shape template 1 shown in Fig. 8 with an equivalent diameter of 0.2 m. The same contact properties as listed in Table 2 are used for this example.

The results of the rockfall test are summarized in Fig. 15. As can be seen from Fig. 15, there are clear differences between FS-DEM and ODEC results, both in terms of particle trajectories and in energy evolutions. This is because FS-DEM and ODEC differ in how irregular-shaped particles are represented and how contact features are resolved. For irregular-shaped particles, these two aspects would impact the particle response during each collision, and such impacts may accumulate during the simulation, eventually leading to the differences between FS-DEM and ODEC observed in Fig. 15. As to the particle energy, case II shows more differences between the two methods than case

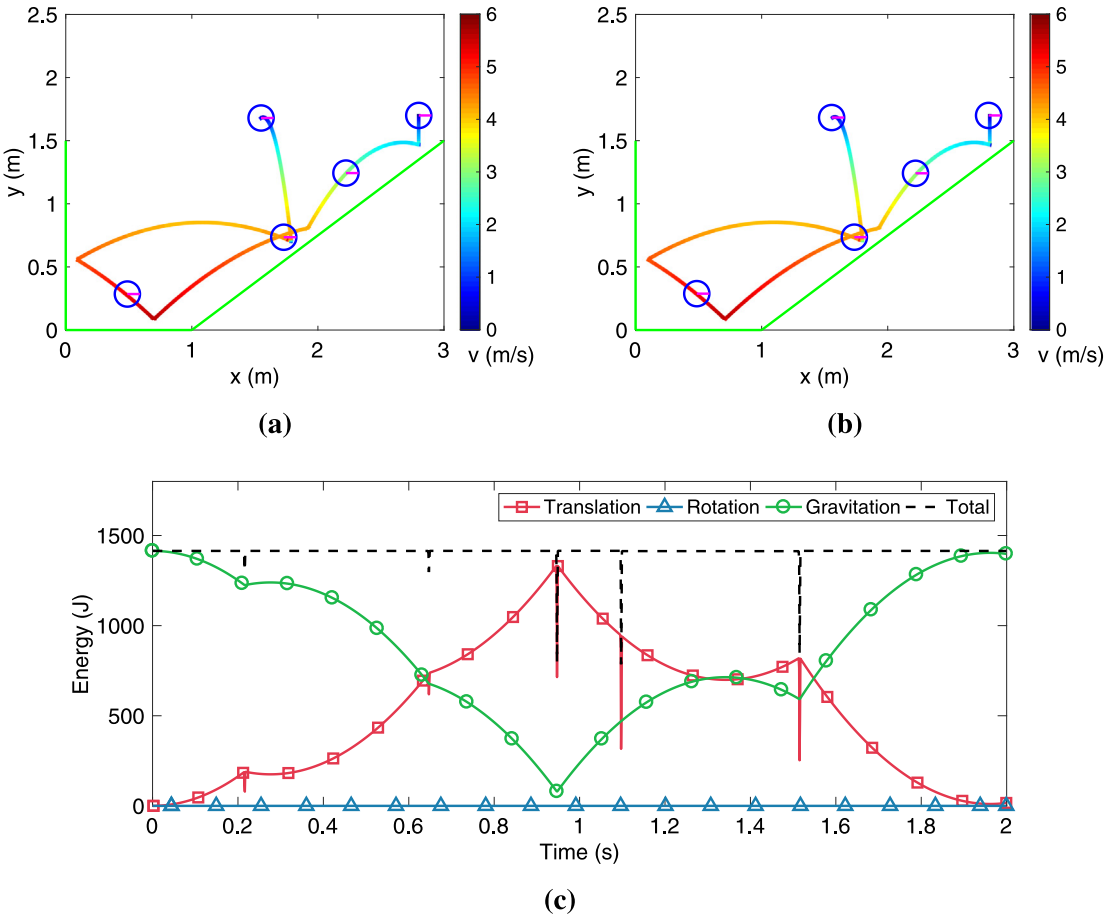

Fig. 13. Disc-shaped single-particle rockfall simulation — case I (i.e., no contact friction and damping): (a) particle trajectory simulated in FS-DEM, (b) particle trajectory simulated in PFC, and (c) the energy evolution evaluated in FS-DEM. Snapshots of the particle (blue circle) in (a) and (b) are taken at 0, 0.5, 1.0, 1.5, and 2.0 s. The trajectory is colored by the particle velocity (unit: m/s). (For interpretation of the references to color in this figure legend, the reader is referred to the web version of this article.)

I and case III. This can be partially attributed to the fact that case I is energy-conservative and case III dissipates energy quickly due to the damping effects.

The effects of particle shape irregularity can be observed from comparisons between Figs. 13–15. In case I, the disc-shaped particle does not exhibit any rotations during the simulation, while the irregular-shaped particle does. The rotational energy of the irregular-shaped particle is obtained from the rotational moment as a result of contact forces not passing the particle centroid. In cases II and III, it can be observed that a greater amount of energy is dissipated in the irregular particle rockfall test compared to that of a disc-shaped particle.

It should be noted that although there are differences between the results of FS-DEM and ODEC, both of them are correct on the basis of their specific implementations. This can be verified from the observation that the energy is conserved in the scenarios without friction and damping (i.e., case I). To compare the accuracy of FS-DEM and ODEC requires the benchmark results of these rockfall tests, which is not available to the best of the authors' knowledge, and therefore, will not be explored in this work. Nevertheless, as aforementioned, FS-DEM is more efficient in representing irregular shapes and has the advantage that the Fourier coefficients in FS-DEM could be correlated to the shape descriptors of a particle.

5.2.3. Timestep sensitivity study

To provide insights into the sensitivity of the FS-DEM results to timestep sizes, we repeated the rockfall simulations with different timestep sizes. With recourse to Eqs. (31) and (32), the critical timestep is calculated

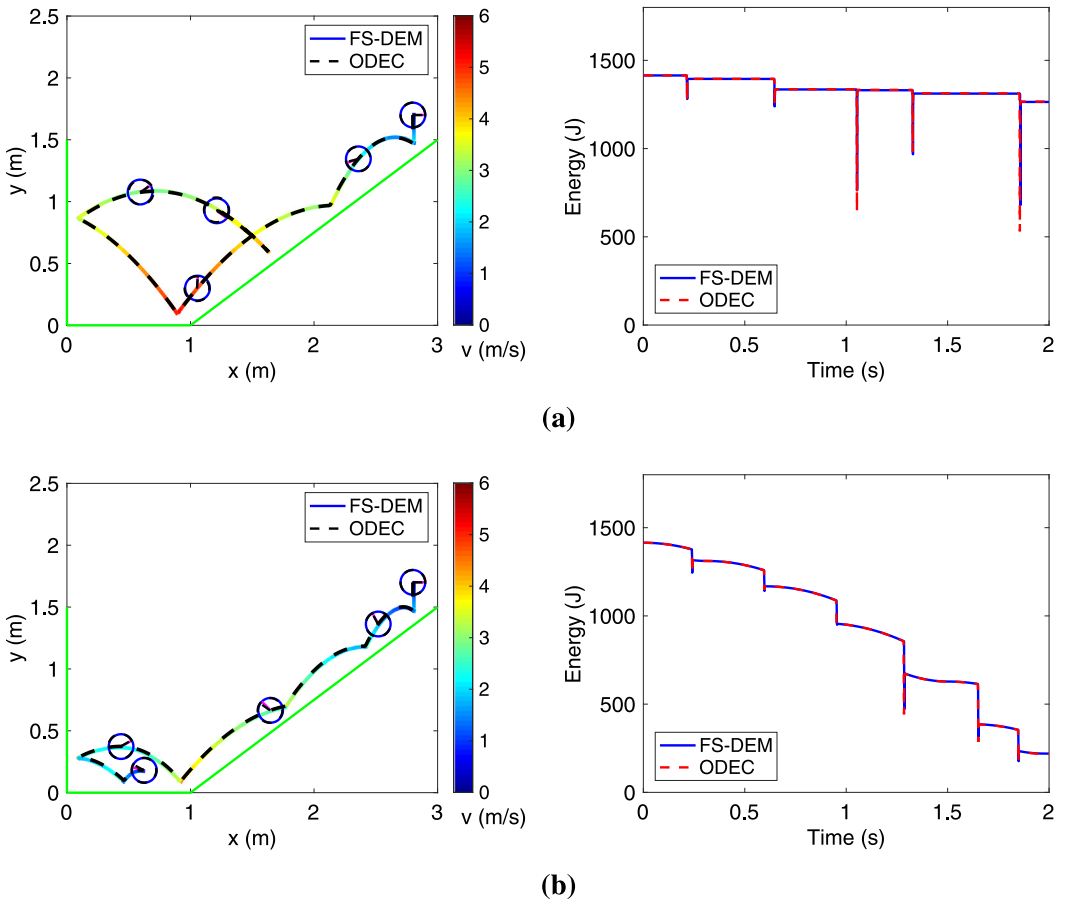

Fig. 14. Particle trajectory and energy evolution in disc-shaped single-particle rock fall test for both FS-DEM and PFC (using the ODEC method): (a) case II (i.e., contact friction 0.2, contact damping 0) and (b) case III (i.e., contact friction 0.2, contact damping 0.2).

to be 1×10^{-3} s using the SDOF-based approaches, and about 2.9×10^{-4} s using the Rayleigh wave speed-based approaches. In Eq. (32), the equivalent particle radius is approximated to be 0.1 m, and the particle shear modulus and Poisson's ratio are estimated from particle normal and shear stiffness [46], where the overlapping distance is assumed to be less than one-tenth of the particle radius to ensure numerical stability.

The results of rockfall simulations with timestep at 5×10^{-5} s, 1×10^{-4} s, 3×10^{-4} s, 1×10^{-3} s, and 2×10^{-3} s are plotted in Fig. 16. For cases with a timestep size much smaller than the critical timestep, the FS-DEM returns almost identical results in terms of both particle trajectory and energy evolution (see Figs. 16(a) and 16(b)). For cases with a timestep size close to the critical timestep, the difference becomes more apparent (see Figs. 16(c) and 16(d)). As for the case with a timestep larger than the critical timestep, the particle may move too much in one increment, which results in spuriously large overlaps that are manifested by the spurious kinetic energy (see Fig. 16(e)).

5.3. Multiple-particle oedometric compression test

To further explore the performance of the FS-DEM, an oedometric compression test of multiple irregular particles is conducted. This test is similar to the classic nine-disc or fifteen-grain tests performed in [5,14]. The test involves three stages of particle behaviors, i.e., (I) deposition, (II) compression and (III) holding.

The rainfall method [52] is adopted for the first stage to generate test specimen. In this stage, a particulate system with 200 particles is first generated using the shape templates shown in Fig. 8. The particles have an equivalent diameter of 0.07 m. They are initially placed in a box container with the particle centroids being spaced 0.14 m

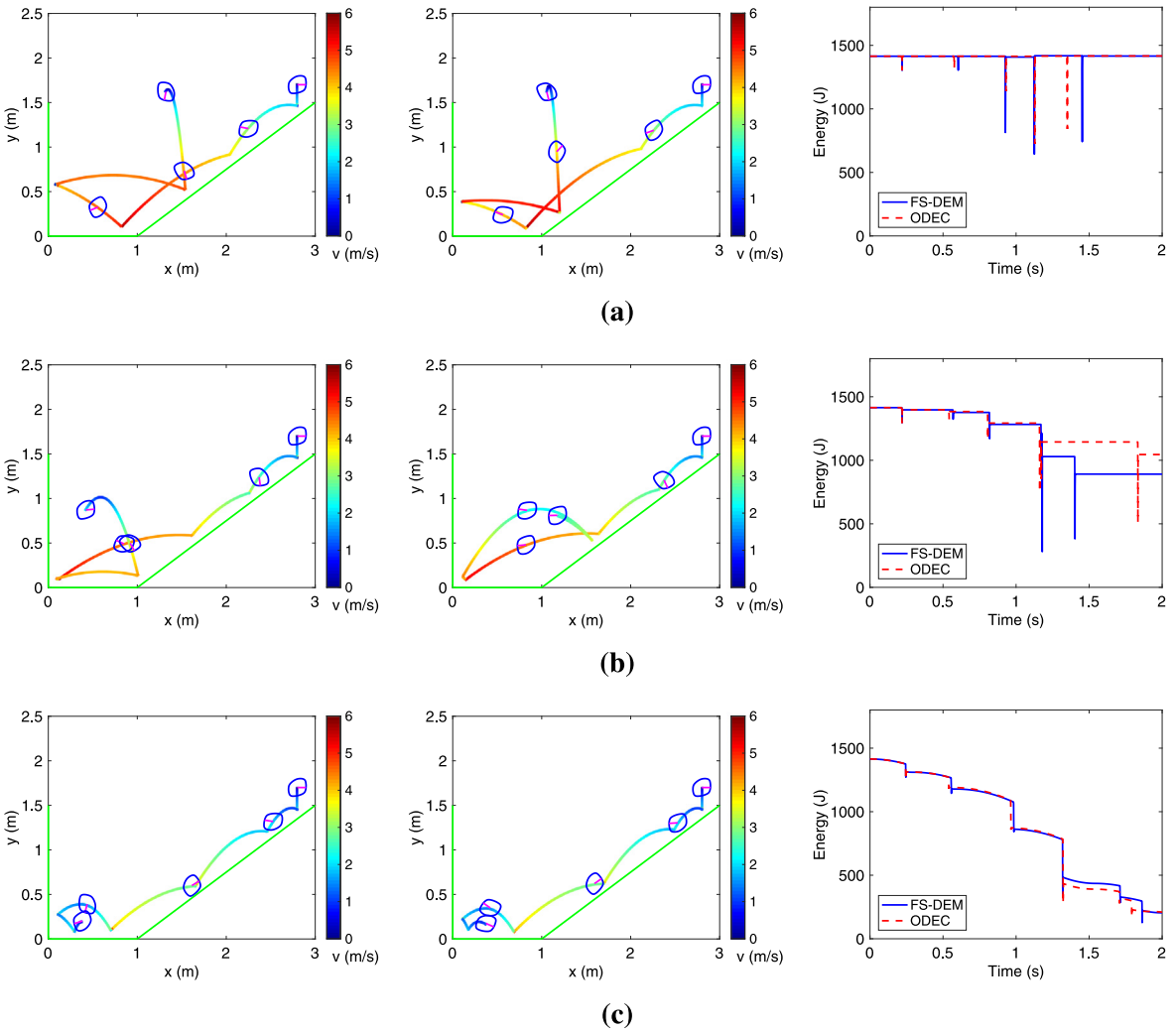

Fig. 15. The particle trajectory and energy evolution in the rockfall process using irregular particle: (a) case I, (b) case II, and (c) case III. The left column shows the particle trajectories simulated from the FS-DEM method, and the middle column shows the particle trajectories simulated from the ODEC method.

apart, as shown in Fig. 17(a). The particles are then allowed to rain down into a container of unit square under the influence of gravity. In this stage, the following parameters are used: particle density is 2700 Kg/m^3, contact normal and tangential stiffness of the particle and boundary are 1.0×10^7 N/m, contact friction is 0, and contact damping is 0.7. The particle deposition process is simulated for 4 s with time step fixed at 1×10^{-4} s, resulting in 40,000 computing cycles in total. Snapshots of particles, presented in Fig. 17, are taken at different time to showcase the particle deposition process. It clearly shows how the particles are raining down and colliding with each other. At the end of the deposition process, a particulate specimen is generated.

In stage II, the specimen is compressed by a top wall, which is gradually moving at a speed of 0.1 m/s. The top wall is initially placed at the height of 0.95 m, right above the highest particle. Meanwhile, the other boundary walls are fixed. This stage is simulated for 1.2 s. In stage III, all walls are held fixed and the particulate specimen is allowed to equilibrate and the process takes 0.8 s. In stages II and III, the contact friction is increased to 0.2 while all other model parameters remain the same as in stage I.

The contact fabrics are important microscopic features that can be directly related to the macroscopic bulk strength of the particle assembly [53–55]. Fig. 18 shows the snapshots of particle packing and contact fabrics at different stages of the compression process. The compression gradually leads to increases of contact overlapping

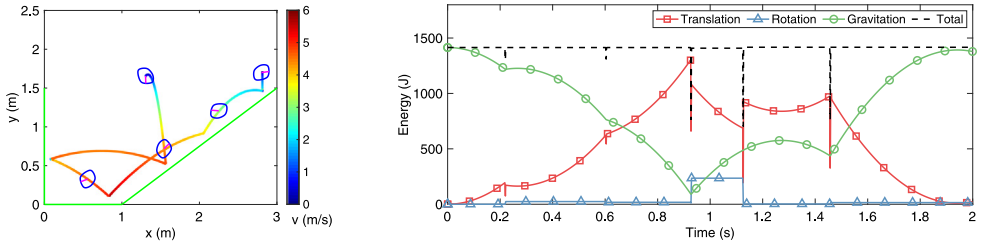

(a) Timestep: 5×10^{-5} s

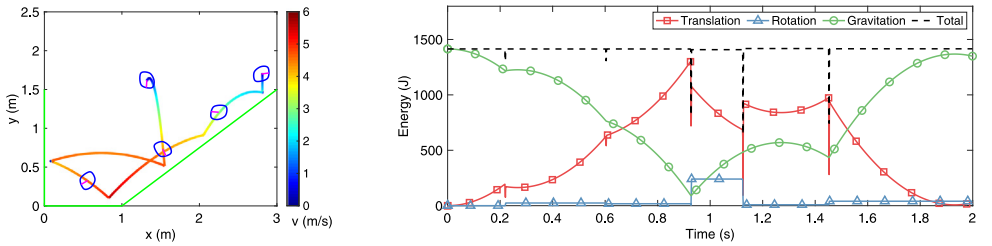

(b) Timestep: 1×10^{-4} s

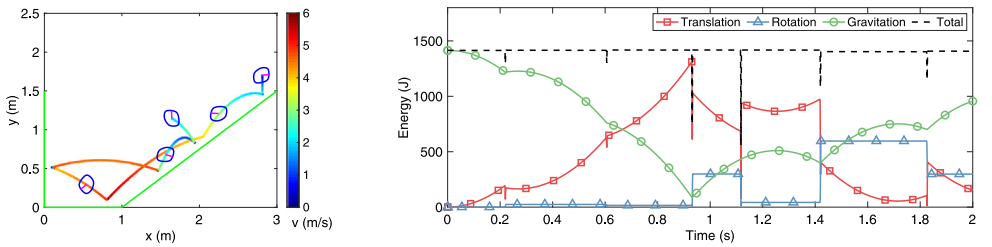

(c) Timestep: 3×10^{-4} s

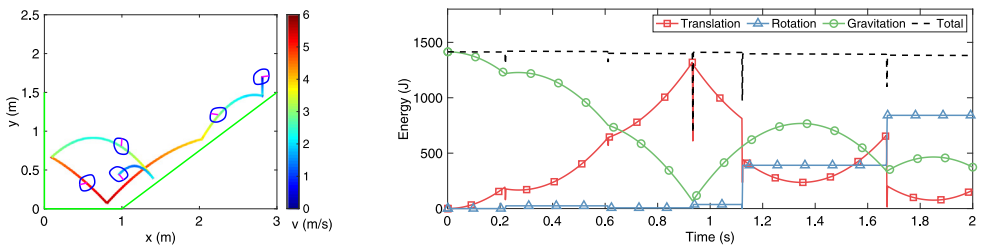

(d) Timestep: 1×10^{-3} s

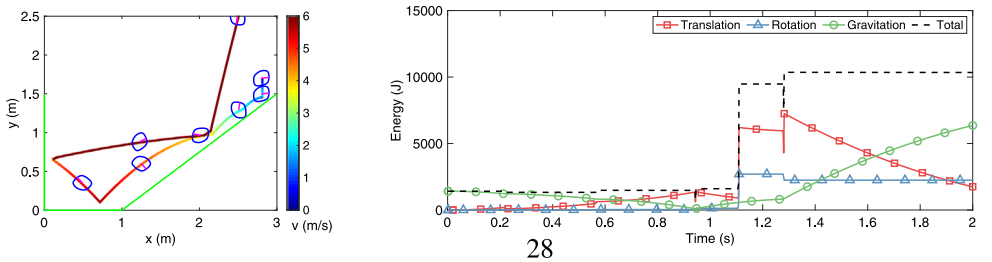

28

(e) Timestep: 2×10^{-3} s

Fig. 16. The particle trajectory (left) and energy evolution (right) in the rockfall process simulated with different timestep sizes: (a) 5×10^{-5} s, (b) 1×10^{-4} s, (c) 3×10^{-4} s, (d) 1×10^{-3} s, and (e) 2×10^{-3} s.

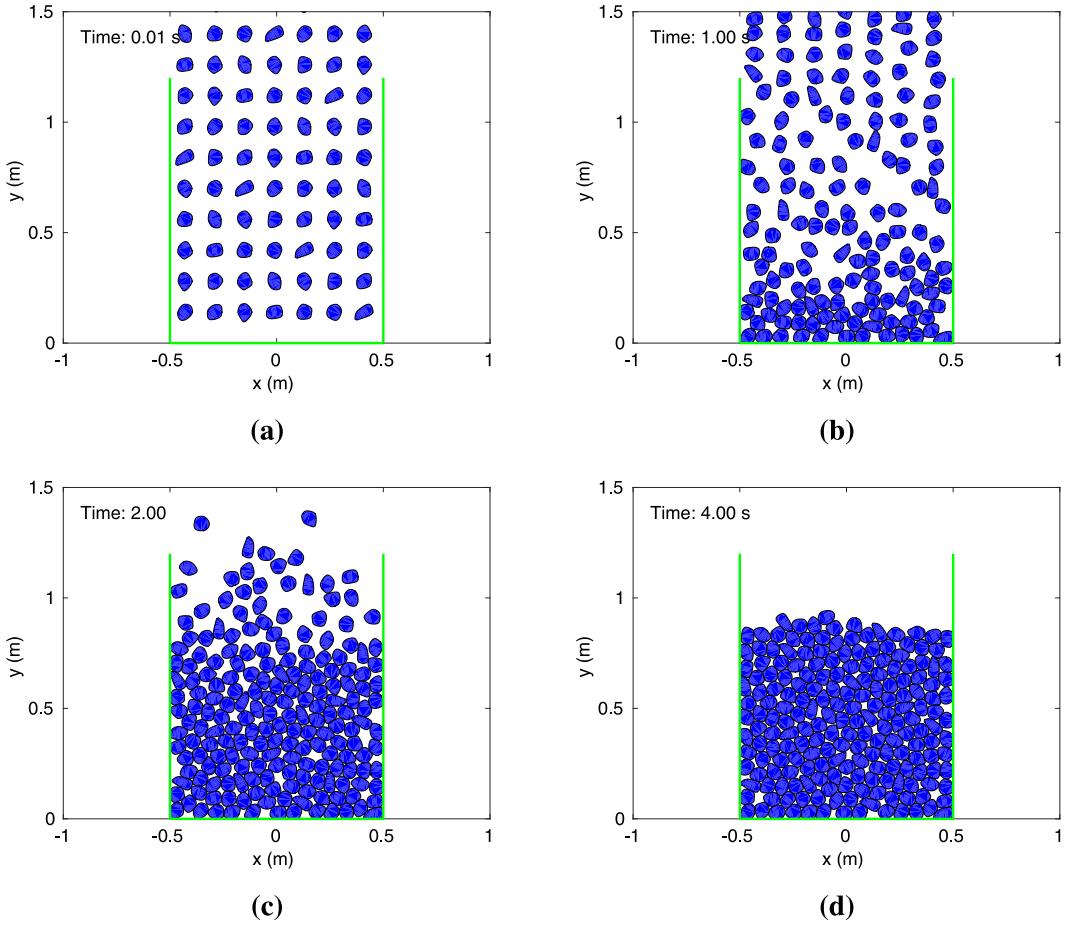

Fig. 17. The snapshots taken at t = 0.01, 1, 2 and 4 s, showcasing the deposition process of the irregular particles.

length, which are captured by the FS-DEM. As the gaps between particles shrink, more contacts are activated. The magnitudes of contact forces also increase as a result of the increasing compressive loading.

The stress profiles of the particle assembly during the compression and holding process are shown in Fig. 19. During the holding process, the stresses remain stable. The performance of the FS-DEM is reflected from the elaborate profile of the stress evolution plots.

6. Summary

In this work, a novel Fourier series-based Discrete Element Method (FS-DEM) is developed for the computational mechanics of irregular-shaped particles. In FS-DEM, a Fourier series-based method is first developed for particle geometric description and coordinate representation. The particle shape descriptors remain constants and independent from particle position or kinematics, which eliminates the need to update the shape descriptors and lead to greater computational efficiency. Using the FS-based particle representation, contact detection and resolution algorithms are then developed to identify contacts and resolving contact features. The FS-DEM method is completed with recourse to conventional contact behavior, laws of motion, and movement integration. Three numerical examples are presented to demonstrate the performance of the proposed method.

In summary, it is found that the FS-based contact detection algorithm is demonstrated to be robust and computationally efficient, especially when a particle shape is described in a higher accuracy (up to four times faster compared to the ODEC-based method for a 99% shape accuracy). In the series of single-particle rockfall simulations, the particle trajectory and energy evolution simulated using FS-DEM coincide with those from a robust commercial

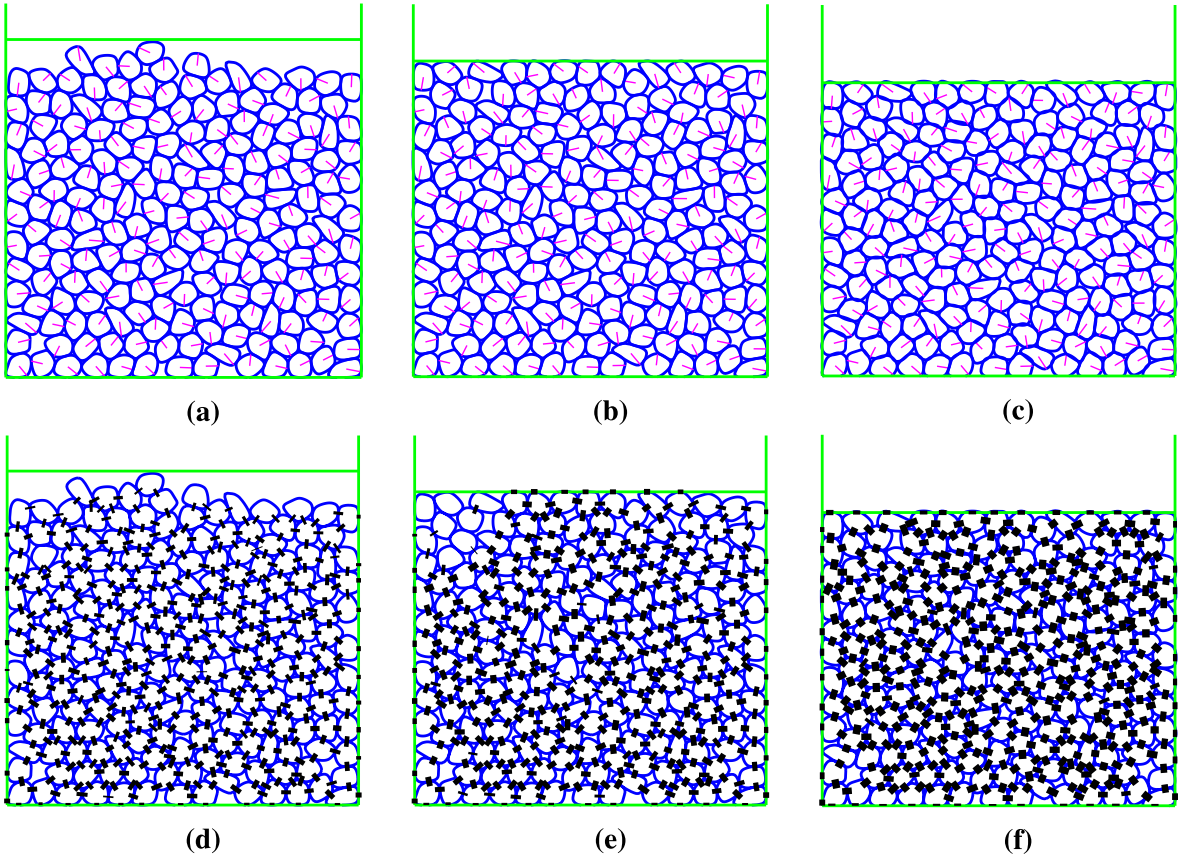

Fig. 18. The particle packing (top) and contact fabrics (bottom) at different stages of the compression process: $\varepsilon = 0\%$ (left), $\varepsilon = 6\%$ (center), and $\varepsilon = 12\%$ (right). The pink lines indicate the particle orientation, and the black thick lines indicate the contact force chain. (For interpretation of the references to color in this figure legend, the reader is referred to the web version of this article.)

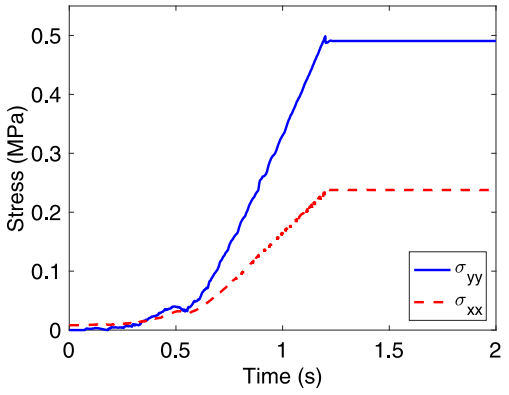

Fig. 19. The stress profiles during the compression (t = 0 ∼ 1.2 s) and holding (t = 1.2 ∼ 2.0 s) process.

DEM code PFC for disc-shaped particles, while noticeable differences are observed for the irregular particle case due to different methods in shape description and contact feature definition. Finally, an oedometric compression test is performed to demonstrate the capability of FS-DEM in capturing particle packing profile, contact fabric,

and stress–strain evolution for multiple irregular-shaped particle systems. Future work will focus on optimizing the computational performance of the prototype code for full-scale simulations, and on extending this framework to three-dimensional problems, with recourse to spherical harmonics to describe particle shapes.

Acknowledgments

The authors would like to acknowledge the supports provided by Clemson University's Support for Early Exploration and Development (CU-SEED) (United States) program and by the National Natural Science Foundation of China Grant (No. 51678578).

Appendix A. Newton's method for contact detection

A.1. Particle–particle contact

The global coordinates of point A_p can be expressed in the FS method, rewritten here as

$$(X_{A_p}, Y_{A_p}) = (X_C + \mathcal{T}^p_{FS}(\vartheta - \theta_0)\cdot \mathcal{C}^p_{FS}\cos(\vartheta), Y_C + \mathcal{T}^p_{FS}(\vartheta - \theta_0)\cdot \mathcal{C}^p_{FS}\sin(\vartheta)) \tag{A.1}$$

where ϑ determines the coordinates of point A_p. The length of line segment C_qA_p is calculated as

$$\mathcal{L}_{C_qA_p} = \sqrt{(X_{C_q} - X_{A_p})^2 + (Y_{C_q} - Y_{A_p})^2} \tag{A.2}$$

Since point A_q is the intersection of the surface of particle q and line C_qA_p, the angle ϑ_{A_q} from positive X-axis to vector $\overrightarrow{C_qA_q}$ can be calculated given the coordinates of points C_q and A_p. Then the global coordinates of point A_q can be expressed as

$$(X_{A_q}, Y_{A_q}) = (X_C + \mathcal{T}^q_{FS}(\vartheta_{A_q} - \theta_0)\cdot \mathcal{C}^q_{FS}\cos(\vartheta_{A_q}), Y_C + \mathcal{T}^q_{FS}(\vartheta_{A_q} - \theta_0)\cdot \mathcal{C}^q_{FS}\sin(\vartheta_{A_q})) \tag{A.3}$$

Thus, the length of line segment C_qA_q is calculated as

$$\mathcal{L}_{C_qA_q} = \sqrt{(X_{C_q} - X_{A_q})^2 + (Y_{C_q} - Y_{A_q})^2} \tag{A.4}$$

Finally the signed distance $\mathcal{D}$, i.e., the particle–particle contact indicator, is calculated as

$$\mathcal{D}(\vartheta) = \sqrt{(X_{C_q} - X_{A_p})^2 + (Y_{C_q} - Y_{A_p})^2} - \sqrt{(X_{C_q} - X_{A_q})^2 + (Y_{C_q} - Y_{A_q})^2} \tag{A.5}$$

The minimization problem (12) can be rewritten equivalently as

$$\frac{\partial \mathcal{D}}{\partial \vartheta}(\vartheta) = 0 \tag{A.6}$$

Eq. (A.6) can be solved via the Newton's method, in which the following numerical derivatives are adopted:

$$\frac{\partial \mathcal{D}}{\partial \vartheta} = \frac{\mathcal{D}(\vartheta + \delta\vartheta) - \mathcal{D}(\vartheta - \delta\vartheta)}{2\delta\vartheta} \tag{A.7}$$

$$\frac{\partial^2 \mathcal{D}}{\partial \vartheta^2} = \frac{\mathcal{D}(\vartheta + \delta\vartheta) - 2\mathcal{D}(\vartheta) + \mathcal{D}(\vartheta - \delta\vartheta)}{\delta\vartheta^2} \tag{A.8}$$

where $\delta\vartheta$ is the infinitesimal variation of ϑ. A grid sampling of the variable ϑ is involved to obtain the reasonable initial guess.

A.2. Particle–boundary contact

Substituting Eqs. (5) and (6) to Eq. (18) gives

$$\mathcal{L}_A = \mathcal{L}_C + r\sin(\alpha - \vartheta_A) \tag{A.9}$$

Problem (20) can be then expressed as

$$\min_{\vartheta_A} \mathcal{P} = \min_{\vartheta_A} \left(\mathcal{L}_C^2 + \mathcal{L}_C r\sin(\alpha - \vartheta_A)\right) \tag{A.10}$$

Since $\mathcal{L}_C^2$, the distance of particle centroid to the wall, is constant in current computational cycle, problem (20) is equivalent to

$$\min_{\vartheta_A} \mathcal{H} = \min_{\vartheta_A} \left(\mathcal{L}_C r \sin(\alpha - \vartheta_A)\right) \tag{A.11}$$

The minimization problem is further converted to

$$\frac{\partial \mathcal{H}}{\partial \vartheta_A} = \mathcal{L}_C \left(\frac{\partial r}{\partial \vartheta_A} \sin(\alpha - \vartheta_A) - r\cos(\alpha - \vartheta_A) \right) = 0 \tag{A.12}$$

where the Jacobian can be calculated by

$$\mathcal{J} = \mathcal{L}_C \left(\frac{\partial^2 r}{\partial \vartheta_A^2} \sin(\alpha - \vartheta_A) - 2\frac{\partial r}{\partial \vartheta_A} \cos(\alpha - \vartheta_A) - r\sin(\alpha - \vartheta_A) \right) \tag{A.13}$$

The first and second derivatives of r with respect to ϑ_A are calculated as

$$\frac{\partial r}{\partial \vartheta_A} = \sum_{n=0}^{N} \left[-n a_n \sin(n\theta) + n b_n \cos(n\theta) \right] \tag{A.14}$$

$$\frac{\partial^2 r}{\partial \vartheta_A^2} = \sum_{n=0}^{N} \left[-n^2 a_n \cos(n\theta) - n^2 b_n \sin(n\theta) \right] \tag{A.15}$$

Appendix B. Intersection of line and particle surface

The intersection N of line and particle surface is found by solving the following equivalent mathematical problem:

$$\mathcal{L}_N = 0 \tag{B.16}$$

where $\mathcal{L}_N$ is the signed distance from point N to line $\overrightarrow{MN}$, which passes the effective contact centroid M and is parallel to the contact normal direction.

This problem can be further expressed as

$$\mathcal{L}_N = \mathcal{L}_C + r\sin(\alpha - \vartheta_N) = 0 \tag{B.17}$$

where $\mathcal{L}_C$ is the signed distance from the particle centroid to the line $\overrightarrow{MN}$, α is the slope angle of the line, and ϑ_N is the variable to be solved, which determines coordinates of point N.

The Jacobian can be calculated by

$$\mathcal{J} = \frac{\partial r}{\partial \vartheta_A} \sin(\alpha - \vartheta_A) - r\cos(\alpha - \vartheta_A) \tag{B.18}$$

References

[1] G. Cho, J. Dodds, J. Santamarina, Particle shape effects on packing density, stiffness, and strength: natural and crushed sands, J. Geotech. Geoenviron. Eng. 132 (5) (2006) 591–602.

[2] A. Peña, R. García-Rojo, H. Herrmann, Influence of particle shape on sheared dense granular media, Granul. Matter 9 (3–4) (2007) 279–291.

[3] A.G. Athanassiadis, M.Z. Miskin, P. Kaplan, N. Rodenberg, S.H. Lee, J. Merritt, E. Brown, J. Amend, H. Lipson, H.M. Jaeger, Particle shape effects on the stress response of granular packings, Soft Matter 10 (1) (2014) 48–59.

[4] Y. Xiao, L. Long, T. Matthew Evans, H. Zhou, H. Liu, A.W. Stuedlein, Effect of particle shape on stress-dilatancy responses of medium-dense sands, J. Geotech. Geoenviron. Eng. 145 (2) (2019) 04018105.

[5] P. Cundall, O. Strack, A discrete numerical model for granular assemblies, Géotechnique 29 (1) (1979) 47–65.

[6] Z. Lai, Q. Chen, Characterization and discrete element simulation of grading and shape-dependent behavior of JSC-1A martian regolith simulant, Granul. Matter 19 (4) (2017) 69.

[7] W. Zhong, A. Yu, X. Liu, Z. Tong, H. Zhang, DEM/CFD-DEM modelling of non-spherical particulate systems: theoretical developments and applications, Powder Technol. 302 (2016) 108–152.

[8] Y. Feng, K. Han, D. Owen, A generic contact detection framework for cylindrical particles in discrete element modelling, Comput. Methods Appl. Mech. Engrg. 315 (2017) 632–651.

[9] B. Nassauer, T. Liedke, M. Kuna, Polyhedral particles for the discrete element method, Granul. Matter 15 (1) (2013) 85–93.

[10] G. D'Addetta, F. Kun, E. Ramm, On the application of a discrete model to the fracture process of cohesive granular materials, Granul. Matter 4 (2) (2002) 77–90.
[11] X. Lin, T. Ng, A three-dimensional discrete element model using arrays of ellipsoids, Géotechnique 47 (2) (1997) 319–329.
[12] J. Ting, M. Khwaja, L. Meachum, J. Rowell, An ellipse-based discrete element model for granular materials, Int. J. Numer. Anal. Methods Geomech. 17 (9) (1993) 603–623.
[13] M. Kuhn, OVAL and OVALPLOT: Programs for analyzing dense particle assemblies with the discrete element method (2006), 2006, http://faculty.up.edu/kuhn/oval/oval.html.
[14] J. Andrade, K. Lim, C. Avila, I. Vlahinić, Granular element method for computational particle mechanics, Comput. Methods Appl. Mech. Engrg. 241 (2012) 262–274.
[15] J. Peters, M. Hopkins, R. Kala, R. Wahl, A poly-ellipsoid particle for non-spherical discrete element method, Eng. Comput. 26 (6) (2009) 645–657.
[16] B. Zhang, R. Regueiro, A. Druckrey, K. Alshibli, Construction of poly-ellipsoidal grain shapes from SMT imaging on sand, and the development of a new DEM contact detection algorithm, Eng. Comput. 35 (2018) 733–771.
[17] R. Kawamoto, E. Andò, G. Viggiani, J. Andrade, Level set discrete element method for three-dimensional computations with triaxial case study, J. Mech. Phys. Solids 91 (2016) 1–13.
[18] N. Das, Modeling three-dimensional shape of sand grains using discrete element method (Ph.D. thesis), University of South Florida, 2007.
[19] C. Shi, D. Li, W. Xu, R. Wang, Discrete element cluster modeling of complex mesoscopic particles for use with the particle flow code method, Granul. Matter 17 (3) (2015) 377–387.
[20] D. Potyondy, P. Cundall, A bonded-particle model for rock, Int. J. Rock Mech. Min. Sci. 41 (8) (2004) 1329–1364.
[21] J. Katagiri, T. Matsushima, Y. Yamada, Simple shear simulation of 3D irregularly-shaped particles by image-based DEM, Granul. Matter 12 (5) (2010) 491–497.
[22] Y. Xia, Z. Lai, T. Westover, J. Klinger, H. Huang, Q. Chen, Discrete element modeling of deformable pinewood chips in cyclic loading test, Powder Technol. 345 (2019) 1–14.
[23] Itasca Consulting Group Inc, PFC – particle flow code, ver. 5.0, 2014, Minneapolis: Itasca.
[24] C. Kloss, C. Goniva, A. Hager, S. Amberger, S. Pirker, Models, algorithms and validation for opensource DEM and CFD–DEM, Prog. Comput. Fluid Dyn. 12 (2–3) (2012) 140–152.
[25] R. Ehrlich, B. Weinberg, An exact method for characterization of grain shape, J. Sediment. Res. 40 (1) (1970).
[26] M. Clark, Quantitative shape analysis: A review, J. Int. Assoc. Math. Geol. 13 (4) (1981) 303–320.
[27] J. Beddow, Morphological analysis of particles and microstructure, in: Key Engineering Materials, Vol.29, Trans Tech Publ, 1988, pp. 677–696.
[28] M. Thomas, R. Wiltshire, A. Williams, The use of Fourier descriptors in the classification of particle shape, Sedimentology 42 (4) (1995) 635–645.
[29] E. Bowman, K. Soga, T. Drummond, Particle shape characterisation using Fourier analysis, Géotechnique 51 (6) (2001) 545–554.
[30] E. Garboczi, Three-dimensional mathematical analysis of particle shape using X-ray tomography and spherical harmonics: Application to aggregates used in concrete, Cem. Concr. Res. 32 (10) (2002) 1621–1638.
[31] B. Zhou, J. Wang, B. Zhao, Micromorphology characterization and reconstruction of sand particles using micro X-ray tomography and spherical harmonics, Eng. Geol. 184 (2015) 126–137.
[32] B. Zhou, J. Wang, Random generation of natural sand assembly using micro X-ray tomography and spherical harmonics, Geotech. Lett. 5 (1) (2015) 6–11.
[33] E. Garboczi, J. Bullard, 3D analytical mathematical models of random star-shape particles via a combination of X-ray computed microtomography and spherical harmonic analysis, Adv. Powder Technol. 28 (2) (2017) 325–339.
[34] D. Su, W. Yan, 3D characterization of general-shape sand particles using microfocus X-ray computed tomography and spherical harmonic functions, and particle regeneration using multivariate random vector, Powder Technol. 323 (2018) 8–23.
[35] D. Su, W. Yan, Quantification of angularity of general-shape particles by using Fourier series and a gradient-based approach, Constr. Build. Mater. 161 (2018) 547–554.
[36] B. Zhou, J. Wang, H. Wang, A novel particle tracking method for granular sands based on spherical harmonic rotational invariants, Géotechnique (2018) 1–23.
[37] R. Eberhart, J. Kennedy, A new optimizer using particle swarm theory, in: Proceedings of the Sixth International Symposium on Micro Machine and Human Science, Vol. 1, New York, NY, 1995, pp. 39–43.
[38] Z. Lai, Q. Chen, Particle swarm optimization for numerical bifurcation analysis in computational inelasticity, Int. J. Numer. Anal. Methods Geomech. 41 (3) (2017) 442–468.
[39] J. Lagarias, J. Reeds, M. Wright, P. Wright, Convergence properties of the Nelder–Mead simplex method in low dimensions, SIAM Journal on optimization 9 (1) (1998) 112–147.
[40] S. Zhao, N. Zhang, X. Zhou, L. Zhang, Particle shape effects on fabric of granular random packing, Powder Technol. 310 (2017) 175–186.
[41] P. Cundall, Computer simulations of dense sphere assemblies, in: Studies in Applied Mechanics, Vol. 20, Elsevier, 1988, pp. 113–123.
[42] E. Dintwa, E. Tijskens, H. Ramon, On the accuracy of the Hertz model to describe the normal contact of soft elastic spheres, Granul. Matter 10 (3) (2008) 209–221.
[43] M. Jiang, H. Yu, D. Harris, A novel discrete model for granular material incorporating rolling resistance, Comput. Geotech. 32 (5) (2005) 340–357.
[44] L. Verlet, Computer "experiments" on classical fluids. I. Thermodynamical properties of Lennard-Jones molecules, Phys. Rev. 159 (1) (1967) 98.

[45] M. Otsubo, C. O'Sullivan, T. Shire, Empirical assessment of the critical time increment in explicit particulate discrete element method simulations, Comput. Geotech. 86 (2017) 67–79.
[46] X. Tu, J. Andrade, Criteria for static equilibrium in particulate mechanics computations, Internat. J. Numer. Methods Engrg. 75 (13) (2008) 1581–1606.
[47] R. Hart, P. Cundall, J. Lemos, Formulation of a three-dimensional distinct element model–Part II. Mechanical calculations for motion and interaction of a system composed of many polyhedral blocks, Int. J. Rock Mech. Min. Sci. Geomech. Abstr. 25 (3) (1988) 117–125.
[48] C. Thornton, Numerical simulations of deviatoric shear deformation of granular media, Géotechnique 50 (1) (2000) 43–53.
[49] Y. Li, Y. Xu, C. Thornton, A comparison of discrete element simulations and experiments for 'sandpiles' composed of spherical particles, Powder Technol. 160 (3) (2005) 219–228.
[50] Z. Lai, Q. Chen, Reconstructing granular particles from X-ray computed tomography using the TWS machine learning tool and the level set method, Acta Geotech. 14 (1) (2019) 1–18.
[51] J. Zheng, R.D. Hryciw, A corner preserving algorithm for realistic DEM soil particle generation, Granul. Matter 18 (4) (2016) 84.
[52] J. Härtl, J. Ooi, Numerical investigation of particle shape and particle friction on limiting bulk friction in direct shear tests and comparison with experiments, Powder Technol. 212 (1) (2011) 231–239.
[53] F. Da Cruz, S. Emam, M. Prochnow, J.-N. Roux, F. Chevoir, Rheophysics of dense granular materials: Discrete simulation of plane shear flows, Phys. Rev. E 72 (2) (2005) 021309.
[54] R. Hurley, J. Andrade, Friction in inertial granular flows: competition between dilation and grain-scale dissipation rates, Granul. Matter 17 (3) (2015) 287–295.
[55] X. Li, Y. Dafalias, Constitutive modeling of inherently anisotropic sand behavior, J. Geotech. Geoenviron. Eng. 128 (10) (2002) 868–880.